WATER TRANSPORT ACROSS A POLYMER ELECTROLYTE MEMBRANE UNDER THERMAL GRADIENTS

Richard S. Fu[a], Joshua S. Preston[a], Ugur Pasaogullari[a,*],

Takeshi Shiomi[a,b], Shinichi Miyazaki[b], Yuichiro Tabuchi[b],

Daniel S. Hussey[c], David L. Jacobson[c]

[a] Department of Mechanical Engineering and Center for Clean Energy Engineering,

University of Connecticut, Storrs, CT 06269-5233, USA

[b] Nissan Motor Co. Ltd., Nissan Research Center, Kanagawa 237-8523, Japan

[c] Physics Laboratory, National Institute of Standards and Technology, Gaithersburg, MD

20899-1070, USA

A full-length technical paper submitted to

Journal of Electrochemical Society

July 20, 2010

* Corresponding Author: Phone: (860) 486-9441

Fax: (860) 486-8378

E-mail: ugurpasa@engr.uconn.edu

Abstract

A fundamental experimental and numerical study of the water transport across a perfluorosulfonic acid (PFSA) membrane under a temperature gradient is presented. The water transport phenomenon was experimentally investigated through water flux measurement and neutron radiography. The experimental observations found that water is transported in the direction from the high temperature side to the low temperature side, when both sides of the membrane are sufficiently humidified, and suggest the transport mechanism is concentration gradient driven. The neutron radiography measurements detected the presence of water content gradient across the membrane and higher water content is seen at a larger thermal gradient. A numerical model was developed to investigate the experimental results. Water transport predictions agreed qualitatively but more accurate material and transport property characterizations are needed for further improvement.

Keywords: PEFC, Water Transport, Neutron Radiography, Numerical Simulation

1 Introduction

High current density operation is desirable in automotive and portable applications of polymer electrolyte fuel cells (PEFCs) in particular to minimize the size and weight of the system balance of plant. However, the resulting heat generation due to high overpotentials, predominantly in the cathode catalyst layer, and the Joule heating especially in the electrolyte, cause a temperature gradient across the polymer electrolyte membrane (PEM) as well as in gas diffusion media (GDM). An experimental measurement of the temperature difference of nearly 2 K between the membrane-electrode-assembly (MEA) and the bipolar plates with 1.0 K differential across the MEA at current density of 0.6 A/cm^2 has been reported [1]. The nonisothermal nature of the PEFC contributes to a localized dry-out of the PEM which leads to a deterioration of performance even when the inlets are sufficiently humidified. On the other hand, during low temperature operation, such as during a start-up, the temperature gradient can also induce unwanted condensation of water in the GDM, a condition known as flooding, which impedes the transport of reacting species. Similarly, temperature differential across the GDM can occur during the shut-down process. Thus, establishing a proper water and thermal management is essential for an optimized performance of PEFCs and has been an intensely studied subject over the years; therefore, the present paper aims to understand the description of water transport across a nonisothermal membrane.

Water transport across the PEM is known to occur by several driving modes, which include electric potential, water concentration gradients, and hydraulic pressure gradients. In addition to the aforementioned transport modes, water transport in the through-plane direction induced by the presence of a thermal gradient across the PEM has been known to exist for some time but attention toward the phenomenon in PEFCs has been mostly nonexistent in the literature until recently. The few investigators who studied this phenomenon, however, arrived at various conclusions on the mechanism of the transport.

The transport phenomenon known as thermo-osmosis occurs when a membrane separates two electrolyte solutions, including water, at different temperatures. Tasaka and co-workers reported some of the early works on the water transport through charged and non-charged polymeric membranes under a temperature gradient [2]. They found water travels across the membranes by thermo-osmosis and theorized the mechanism of thermo-osmosis based on a nonequilibrium thermodynamic analysis [3]. They observed the solvent being transferred through a hydrophilic polymer membrane from the cold to the hot side, and in case of a hydrophobic polymer membrane, the water transported was from the hot side to the cold side. A temperature polarization effect, where the effective temperatures at the interfaces of a membrane are different from the temperatures of the bulk solutions, was estimated by measuring the thermal membrane potential.

Quantitative measurements of the thermo-osmotic transfer of pure water, pure methanol, and a water-methanol mixture across Nafion® 117[1] as a function of the temperature difference were carried out by Villaluenga et al. [4]. They found the transport direction to be always from the cold side to the hot side. Based on their reported thermo-osmotic coefficient, the flux is estimated to be around 7.5×10^{-6} kg m^{-2} s^{-1} at a mean temperature of 26.5 °C and with ΔT = 10 °C. Their results indicated that the water flux increases linearly with the gradient of temperature and exhibits an Arrhenius-type relationship to the mean temperature of the membrane. The temperature polarization effect was deemed negligible in their setup due to the bulk fluid motion.

---

[1] Certain trade names and company products are mentioned in the text or identified in an illustration in order to adequately specify the experimental procedure and equipment used. In no case does such identification imply recommendation or endorsement by NIST, nor does it imply that the products are necessarily the best available for this purpose.

Zaffou et al. reported water transport measurements across membranes subjected to a 1 K temperature difference in a liquid-filled fuel cell setup using water-saturated porous separator plates to maintain temperature and humidity [5]. Their tested membranes include non-reinforced and polytetrafluoroethylene (PTFE)-reinforced membranes and MEAs. They observed water transport only in the reinforced membranes in the direction of the hot to the cold side. They also attributed the transport mode to be thermo-osmosis and suggested the transport mechanism to be due to a gradient in surface tension induced by the temperature difference. Zaffou et al. also measured thermally-induced water flux in an operating fuel cell with anode and cathode maintained at different temperatures by the water-saturated porous separator plates [6, 7]. They reported a water flux that is comparable in the order of magnitude as the water generation rate at current density of 0.4 A cm^{-2} in the direction of the cold side. While their experiments were conducted in an actual operating fuel cell, deviation of the actual temperature at the membrane from the bulk fluid temperature was not addressed and the flux in relation to it is unknown.

Most recently, Kim and Mench [8] also arrived at conclusions similar to those of Villaluenga et al. They concluded that the water flux due to thermo-osmosis is in the direction from the cold to the hot side of the membrane, and is proportional to the temperature gradient. They suggested that it exhibits Arrhenius behavior with the average temperature of the membrane and found the flux to be higher in membranes with lower equivalent weight and decreased thickness [9]. Their investigation also included the effects of hydrophobicity of GDM. They determined that the direction of water transport to be from the cold side to the hot side due to thermo-osmosis dominating with hydrophilic GDM, and to be from the hot side to the cold side with hydrophobic GDM, since water transport by phase-change-induced (PCI) flow in porous diffusion media dominates over thermo-osmosis in the membrane. They suggested that the existence of a gas-phase on either side of the membrane affects the direction of the overall flux. In their experiments, non-reinforced membranes had a slightly higher water flux than reinforced membranes, which suggested that the net water flux can be affected by the diffusion mode in the membrane; therefore, they concluded the thermally induced water transport in the PEFC condition is a net result of the flux contributions from the PCI flow in the porous media and the mass diffusion mode in the membrane. They followed up the flux measurements with neutron radiography experiments to visualize the PCI flow in the porous media.

This paper presents our own investigation of water transport across a nonisothermal membrane. Water flux across a membrane that is subjected to a temperature gradient is measured by a water balance experiment. In addition, visualization of water distribution in the through-plane direction by high-resolution neutron radiography (NR) imaging and numerical analyses are performed. Numerical models are developed based on known transport phenomena in the membrane and porous media, and the predictions from the model are directly compared with experimentally obtained results to verify some of the claims made by earlier investigators as well as to draw our own conclusions. Capabilities and limitations of the experimental and numerical analyses are discussed.

2 Experiments

2.1 Water Balance Measurement

2.1.1 Experimental Set Up

Water flux across a PEM induced by a thermal gradient was experimentally measured in single-cell fuel cell hardware. The membrane selected was a Nafion membrane (NAF NE-1110; nominal thickness of 254 μm) without catalyst layers, which was placed in between untreated Toray gas diffusion media (TGP-H-120; nominal thickness of 370 μm) and compressed with 300 μm thick PTFE gaskets in between carbon flow-field plates. (Thick materials were selected to keep the dimension of the components consistent with the NR experiment described in the following section.) The flow-field is a straight flow path, the channel and land widths are 0.2 mm, and the effective area is 25 cm^2. As illustrated in Figure 1, the temperatures of the plates were monitored by embedded K-type thermo-couples and controlled with independent coolant fluid loops. In subsequent discussions, the higher and lower temperatures are referred to as the "hot side" temperature, T_H, and the "cold side" temperature, T_C, respectively.

--

Figure 1

--

Nitrogen gas streams of various humidity were fed into both of the flow-fields at a high flow rate of 10 L min^{-1} in order to minimize variation in the flow direction. At the outlet of each side, the gas stream was passed through a condenser and the exhaust was vented at a constant temperature. The condensate was collected from each side and the rate of water accumulation was measured.

For each side of the flow loop, the rate of water transport across the PEM can be evaluated from the differential of the mass flow rates of the inlet and the outlet:

$$\Delta \dot{m}^C = \dot{m}_{in}^C - \dot{m}_{out}^C \tag{1a}$$

$$\Delta \dot{m}^H = -\dot{m}_{in}^H + \dot{m}_{out}^H \tag{1b}$$

where the superscripts C and H denote the cold side and the hot side, respectively, and the subscripts indicate the inlet (in) and the outlet (out). The mass flow rates of humidified gases at the inlets and the outlets were independently measured in two steps. The mass flow rates at the outlets were measured with the 3-way valves with Port 1 open and Port 2 closed and expressed by

$$\dot{m}_{out(in)} = \frac{M^{H_2O}}{M^{N_2}} \frac{p^{sat}}{P - p^{sat}} \dot{m}^{N_2} + \rho^{H_2O} \dot{V} \tag{2}$$

where M^x is the molecular mass of species *x*, $\dot{m}^{N_2}$ is the mass flow rate of the dry gas (*i.e.* N_2), *P* is the outlet pressure, p^{sat} is the vapor saturation pressure at the outlet temperature, and $\dot{V}$ is the rate of volumetric increase of the condensate. The mass flow rates of the inlets were separately measured in a similar manner; by bypassing the cell by switching the valves to Port 2 and closing Port 1 and correcting for the pressure drop in the cell. The reported water flux across the PEM is the average of the hot side and the cold side gas loops given by Eq. 1. We define water transport from the cold side to the hot side of the membrane as positive, to be consistent with the convention used by earlier investigators [2, 4].

The temperatures of the plates were maintained at $T_H = 74.2 \pm 0.1$ °C and $T_C = 35.5 \pm 0.1$ °C. The relative humidity (RH) of the hot side inlet gas was varied while the RH of the cold side was fixed at 100 %. By applying a temperature gradient, water is expected to reach a saturated condition in the hot side GDM above a certain RH. Such a condition of the PEM simulates the nonisothermal water transport condition less electro-osmotic drag during PEFC operations.

2.2 Water Distribution Measurement with Neutron Radiography

2.2.1 Neutron Radiography in PEFC

Neutron radiography (NR) has become a popular method for the non-invasive visualization and measurement of the liquid water distribution in operating PEFCs. While other *in situ* visualization techniques, including X-ray imaging and magnetic resonance imaging (MRI) are currently being developed, there are many challenges in imaging typical PEFCs. The primary difficulty with X-ray imaging lies in weak attenuation by water in comparison to typical hardware used. In MRI, the difficulty arises in the conductive shell of PEFCs acting as a shield of the pulsed magnetic field and nuclear resonance signal. In contrast, an inherent advantage of NR over other *in situ* water visualization methods is the large scattering cross-section of neutrons by hydrogenous materials while common materials (such as aluminum and carbon) used in PEFC hardware, are relatively transparent [10].

The neutron attenuation is modeled by the Lambert-Beer Law,

$$I = I_o \exp(-\mu t), \tag{3}$$

where I is object image, I_o is a reference state image, μ is a pre-determined attenuation coefficient, and t is the thickness of the object, which in our case is water, assuming beam hardening effect is negligible [10]. (Beam hardening, due to a neutron energy dependent scattering cross-section, is incorporated in the analysis as a second order term in material thickness.)

The sharpness of an imaging system can be characterized by the point spread function (PSF). Two primary contributions to the image unsharpness (blur) come from the beam geometry and the detection mechanism. If each contribution is characterized by a PSF that is assumed to be isotropic, independent, approximately Gaussian, and quantifiable by its standard deviation, the standard deviation of the imaging system σ_i is given by

$$\sigma_i^2 = \sigma_g^2 + \sigma_d^2 . \tag{4}$$

where the subscripts g and d refer to the geometry and detector, respectively. The geometric unsharpness, λ_g, is the full-width-at-half-maximum (FWHM) of image formation from pinhole optics, and is calculated by

$$\lambda_g = \frac{Dz}{L - z} \approx z\frac{D}{L} \tag{5}$$

where D is the source aperture diameter, z is the distance of the sample from the detector, and L is the distance of the neutron source and the detector ($L >> z$). λ_g is approximately related to the standard deviation by

$$\sigma_g \approx \frac{\lambda_g}{2.35} . \tag{6}$$

Image blurring from the detector is often determined from the imaged width of a sharp edge, which is modeled by an error function. Finally, image spatial resolution is traditionally defined as 10 % contrast of the modulation transfer function (MTF) value, which is the Fourier transform of the PSF, given by

$$\delta_i = \frac{\pi \sigma_i}{\sqrt{2 \ln(10)}} . \tag{7}$$

A number of researchers have extensively used NR to investigate the effects of flow-field on the in-plane distribution of water content in PEFCs using ZnS scintillators doped with ^{6}Li imaged onto an amorphous-silicon (aSi) detector [11-18]. The aSi detector at the National Institute of Standards and Technology (NIST) has a pixel pitch of 0.127 mm and a spatial resolution of approximately 0.25 mm [10]. The visualization allowed investigators to determine the sections along the direction of the channel flow that were likely flooded with water under different operating conditions. While aSi detectors are suitable for the in-plane imaging of water distribution, a finer resolution was needed for the through-plane distribution due to PEFC subcomponent thicknesses in the order of magnitude of tens of micron meters.

The first effort to measure the through-plane water distribution in a PEM was made by Bellows et al. [19]. They measured water content in a 4-layer Nafion® 117 membrane composite but were limited to a qualitative measurement due to 50 μm resolution, and slow event reconstruction (about 1 kHz). In recent years, a high-resolution micro-channel plate (MCP) detector doped with ^{10}B and Gd, which has a measured intrinsic resolution of 25 μm, was introduced and made water measurement in the through-plane direction possible with a greater accuracy [20]. A handful of researchers have utilized the high-resolution detector in PEFC applications. Hickner et al. reported the cross-sectional liquid water distribution of an operating fuel cell under various temperature and hydration conditions [21]. Weber and Hickner used a pseudo-two-dimensional numerical model to obtain qualitative fits to the shape of the measured liquid water profiles rather than quantitatively. They determined that a strong PCI flow exists and can significantly impede oxygen transport on the cathode [22]. Spendelow et al. used NR to quantify liquid water distribution in the MEA and GDLs in axial direction of the gas flow [23]. Turhan et al. investigated the effects of hydrophobicity of channel walls on the through-plane liquid water storage, transport, and flooding mechanism [24].

2.2.2 Neutron Radiography Experimental Setup

A specially designed cell was prepared for the through-plane visualization of water distribution inside of a PEFC subjected to a temperature gradient. The hardware shown in Figure 2 is a gold-coated aluminum alloy 6061 end plate with a machined flow-field positioned 5 mm from the detector-side edge to minimize λ_g. A non-reinforced Nafion® (NE-1100; 254 μm) is placed between untreated Toray gas diffusion media (TGP-H-120; 370 μm) and the composite is compressed together with 300 μm PTFE gaskets by the plates. No catalyst layer was applied; thus, only the water transport behavior of the PEM and the GDM were sought. A thick membrane was selected in order to compensate for the finite image spatial resolution.

--

Figure 2

--

The flow-field is a 1.0 mm width single serpentine flow channel, which is designed to minimize pressure drop in an attempt to achieve uniform flow conditions across the cell. The dimensions of the area to be measured have a height of 14 mm and a depth of 6 mm in the direction of neutron transmission. Nitrogen gas streams were supplied to both flow-fields at the flow rate of 100 sccm to minimize the variation in the flow direction to ensure differential cell conditions. The end plates were embedded with cartridge heaters to independently control the temperature of each plate to within ±0.5 K of the target temperatures. Humidifier temperatures were set to maintain the gases at a constant humidity for each set of experimental conditions. The hot-side gas RH was varied from 40 %, 64 %, and 95 %, while the cold-side humidity was kept constant at 95 % RH at the given plate temperature. The inlet gases were additionally heated to prevent any vapor from condensing in the lines. The cell temperature gradients as well as the dew point temperature conditions are described in Table 1. All NR experiments reported in this paper were carried out at the Neutron Imaging Facility at the National Institute of Standards and Technology (NIST) Center for Neutron Research.

--

Table 1

--

A micro-channel plate (MCP) detector with an intrinsic spatial resolution of 25 μm was used for the through-plane imaging [10]. The accuracy of water thickness measurement in NR is limited by the random uncertainty due to the detected number of neutrons and systematic uncertainty arising from the sample misalignment to the beam or scattering from thick columns of liquid water [10]. In order to reduce the random uncertainty (*i.e.* increasing the signal-to-noise ratio) due to the neutron counting statistics, each wet image was acquired for 60 s and then 50-60 raw images were averaged at each RH condition. Since the MCP detector is susceptible to the background gamma field, a background image was subtracted from the raw intensity images. Finally, the averaged wet images were divided by the corresponding averaged dry reference images in order to calculate water thickness inside of the cell according to the Lambert-Beer law (Eq. 3) with the pre-determined neutron attenuation coefficient of 0.338 mm^{-1}. Here, the wet images refer to the images taken under humidified gas condition and the dry images refer to the images taken under non-humidified gas conditions. We note that the dry reference state images were taken at a condition that was limited by the capability of the test stand at the time. Although the gases bypassed the saturators, a check-valve was not in place at the outlet of the saturator, and it is possible that vapor may arise from the piping of the saturators. Therefore, the present study considers the reference state to be at a humidity level where the saturators are at the ambient temperature of about 23 °C. The measured water thickness was then averaged to give a thickness profile in the through-plane direction with reduced uncertainties. Due to the thickness of the components, at least a 180 minute interval was given in between each experimental condition to allow time to develop steady-state conditions prior to imaging. The specifications of the NR experiments are summarized in Table 2.

--

Table 2

--

2.3 Numerical Model

In order to complement findings from the experimental procedures described in the above sections, a one-dimensional (1-D), two-phase, nonisothermal model based on the Multiphase-Mixture (M^2) model developed by Wang and Cheng [25, 26] and adapted for PEFCs [27-29] was employed. The 1-D model allows interpretation of the results from the experiments quickly and with few convergence or stability problems. The model is used to predict water content in the PEM and water saturation in the GDM and resulting water flux.

2.3.1 Model Assumptions and Governing Equations

The modeling domain consists of a one-dimensional representation of the GDM-PEM-GDM experimental cell layers. The domain is given boundary conditions of the respective hot and cold-side temperature and RH according to Table 1, which are represented as the conditions at the GDM-plate interfaces. Although the interfaces of the GDM-plate are two-dimensional in actuality, due to the large thermal mass of the aluminum plates, the flowing gases are assumed to be in thermal equilibrium with the respective plate and the in-plane temperature variation at the interface essentially vanishes. It is also assumed that no liquid water is present at the boundaries. According to the two-dimensional numerical analysis by Kim and Mench [8], temperature uniformity at the PEM-GDM interfaces is achieved with the presence of GDM; thus further validating the use of a 1-D model. For simplicity, the thermal contact resistances at the interfaces are considered negligible in the present study. Further, saturated vapor pressure is assumed to be in equilibrium with the local temperature.

Table 3

The governing equations solved are conservation equations of mass, species, and energy summarized in Table 3. The mass conservation equation for a steady-state, two-phase mixture is given by Eq. 8 where u is the superficial mixture velocity and ρ is the mixture density defined as

$$\rho = s\rho_l + (1-s)\rho_g \,. \tag{13}$$

The volume fraction of liquid water phase occupying the pores of the diffusion media is denoted by s and vapor phase is given by 1-s.

Eq. 9 and Eq. 10 respectively describe the species and energy equations of the M^2 formulation in the diffusion media. The term on the left hand side of Eq. 9 represents the advective transport with the mixture-phase velocity. The gas and liquid phases have different velocities; therefore, the advective transport of the two-phase mixture is corrected by an advection correction factor, γ_c:

$$\gamma_c = \frac{\rho}{C_{\mathrm{H_2O}}}\left(\frac{\lambda_l}{M_{\mathrm{H_2O}}} + \frac{\lambda_g C^g_{\mathrm{H_2O}}}{\rho_{\mathrm{g}}}\right) \quad \text{for } \mathrm{H_2O} \tag{14}$$

$$\gamma_c = \frac{\rho\lambda_g}{\rho_g(1-s)} \qquad \text{for } \mathrm{N_2} \tag{15}$$

Where the mobility of each phase, λ_k, is given by

$$\lambda_k = \frac{k_{rk}/\nu_k}{\sum k_{rk}/\nu_k}, \ \sum \lambda_k = 1 \,. \tag{16}$$

The relative permeability of individual phases, k_r, is defined as the ratio of the intrinsic permeability for phase k at a given saturation to the total intrinsic permeability of the porous medium. In general, it is assumed to have a fourth power relation [30] to the phase saturations as

$$k_{rl} = s^4, \qquad k_{rg} = (1-s)^4 \,. \tag{17}$$

The second term on the right hand side of Eq. 9 describes the capillary transport and the liquid flux, j_l, is given by

$$j_l = \frac{\lambda_l \lambda_g}{\nu} K \frac{dp_c}{dx} \tag{18}$$

where, the capillary pressure is

$$p_c = \sigma \cos\theta_c \left(\varepsilon/K\right)^{1/2} J(s). \tag{19}$$

The Leverett *J*-function, *J*(*s*), is adopted for this study and for hydrophilic untreated carbon paper GDM (*i.e.* $\theta_c < 90°$) it is described by [27]

$$J(s) = 1.417(1-s) - 2.120(1-s)^2 + 1.263(1-s)^3. \tag{21}$$

The third term on the right hand side of Eq. 9 describes the water vapor diffusion in the nonisothermal two-phase zone.

The left hand side term in the energy conservation equation given by Eq. 10 similarly corrects the advective transport of energy through the mixture phase via an advection correction factor, γ_h,

$$\gamma_h = \frac{\rho\left(\lambda_l c_{p,l} + \lambda_g c_{p,g}\right)}{s\rho_l c_{p,l} + (1-s)\rho_g c_{p,g}}. \tag{22}$$

The first term on the right hand side of Eq. 10 is heat conduction across the two-phase mixture and solid phase. The last term represents latent heat change due to phase change processes. Energy released or gained due to the membrane water sorption/desorption processes are not considered at present time.

Within the PEM, the conservation equations for water and energy given by Eq. 11 and Eq. 12 are solved. The water transport mode across the PEM is assumed to be predominantly diffusion due to a water concentration gradient. The water uptake by

Nafion® given by Hinatsu et al. [31] at 80 ºC is modified to include a hypothetical liquid water equilibrated uptake that is linearly proportional to the saturation for conditions above $a > 1$.

$$\lambda = \begin{cases} 0.3 + 10.8a - 16.0a^2 + 14.1a^3 & \text{for } 0 \le a \le 1 \\ 9.2 + s \cdot \{[9.38 + 0.138(T - 273.15K)] - 9.2\} & \text{for } 0 < s \le 1 \end{cases} \tag{23}$$

For the water diffusion coefficient in the membrane, the model of Motupally et al. [32] is adopted:

$$D_{\lambda}^{\mathrm{H_2O}} = \begin{cases} 3.10 \times 10^{-3} \lambda \left(e^{0.28\lambda} - 1\right) e^{-2436/T} & \text{for } 0 < \lambda \le 3 \\ 4.17 \times 10^{-4} \lambda \left(161 e^{-\lambda} + 1\right) e^{-2436/T} & \text{for } \lambda \ge 3 \end{cases} \tag{24}$$

Unlike in [4] where the temperature polarization effect was negligible due to bulk fluid flow mixing, the temperature drop across the GDM is significant and it becomes necessary to know the temperature at the PEM-GDM interfaces in a PEFC setup. A separate experiment using the cell hardware described in Section 2.1.1 with a micro-thermocouple (50 µm diameter) inserted in between the cold side GDM and the PEM was conducted, coupled with the numerical model described, to address this issue. Fixing the through-plane thermal conductivity of the PEM to be 0.25 W m^{-1} K^{-1} at 65 ºC and nearly fully-humidified inlet gas [33], the thermal conductivity of the GDM, k_s, under the compression was estimated to be approximately 1.0 W m^{-1} K^{-1} from a temperature differential (ΔT1). These thermal conductivities were further validated by additional temperature gradients, ΔT2 and ΔT3. The calculated value is well within the range of values reported in the literature. The experimentally measured temperatures as well as the numerical predictions are shown in Figure 3.

--

Figure 3

--

In order to approximate the dependence of the effective thermal conductivity of the porous media on liquid saturation, a simple parallel model is adopted,

$$k_{eff} = (1-\varepsilon)\cdot k_s + \varepsilon \cdot \lfloor s \cdot k_l + (1-s)\cdot k_g \rfloor \tag{25}$$

where ε is the porosity of the porous media, k_l and k_g are thermal conductivities of liquid and gas phase fluid, respectively.

The magnitude and direction of water and heat fluxes are initially guessed and solved in each layer until a convergence is attained in water concentration and temperature. The material and transport properties used in the numerical analysis are summarized in Table 4.

--

Table 4

--

While deconvolution of the neutron radiographs with the PSF is possible to enhance water content features, it amplifies the shot noise [35]. A more robust method is to convert the water concentration predictions from the model into equivalent water thickness with the dry reference state correction (at the ambient condition) in reference to the component depth. The equivalent water thickness profile is discretized according to the detector pixel pitch. Convolution of the PSF at each point is carried out based on the estimated spatial resolution, the distance from the neutron source to the detector L, and the distance of the sample to the detector z. The resulting profiles simulate the water content measured in the NR experiment and allow for a direct comparison between numerical predictions and experimentally obtained results by NR.

3 Results and Discussion

3.1 Water Flux Measurement

Numerical prediction of the temperature distribution within the GDM-PEM-GDM composite (bounded by $T_H = 74.2$ °C and $T_C = 35.5$ °C) when both gases are fully humidified predicts a large temperature drop of ~26 K across the PEM. When a temperature gradient is present, the drop in the temperature in the hot side GDM towards the PEM decreases the local vapor saturation pressure, thus increasing the vapor activity at the interface of the membrane. Conversely, the cold side GDM has a higher temperature towards the PEM, thus the vapor activity decreases. Therefore, a vapor activity differential across the membrane is induced, which results in a water content gradient within the membrane and the direction of the water transport and its magnitude depend on the intricate interplay between the temperature and humidity.

The measurement of water flux through the PEM under a thermal gradient is reported in Figure 4. The data points represent averages of the fluxes obtained from the cold-side and the hot-side. As the RH of the hot side gas is increased, the direction of the flux was found to reverse from positive to negative. Therefore, when both of the inlet gases are fully-humidified, the water flux in the PEM in a PEFC setup is in the direction from the hot to the cold. Water flux calculated by the model is plotted together in the solid line in Figure 4. Similarly to the experimental data, the model predicts that the water transport changes its direction from positive to negative as the hot side humidity is increased. An excellent agreement to the experiment is obtained for up to approximately 65 % RH, where water in the cell remains in vapor phase. Above 65 % RH, the model begins to deviate from the experiment. It is believed that saturation occurs in the hot side GDM at those conditions. The deviation of the model at higher RH may be a result of inadequate characterizations of the membrane water content or the transport in the PEM when liquid water is present at the interfaces.

--

Figure 4

--

A direct comparison of thermo-osmotic water flux with our measurement is not straight-forward and difficult since thermo-osmosis transport under partially saturated conditions is unknown. However, when compared to water flux calculated from the thermo-osmositic coefficient reported by Villaluenga et al. [4] at the same temperature difference across the PEM, it is found that the measured water flux is an order of magnitude higher in the opposite direction, despite the large temperature drop and a thicker membrane used in our experiments. When thermo-osmotic diffusivity found by Kim and Mench [8] is used, the calculation yields a comparable flux magnitude but again in the opposite direction. We note that the experimental conditions used by earlier investigators [2, 4, 5, 8], where both sides of the membrane are completely in direct contact with liquid water. We further note that, as described by Eq. 11, the model solves water transport in the PEM only by diffusion and does not incorporate thermo-osmosis. Thus, it suggests that the thermally-induced water transport mechanism across the PEM in a PEFC is fundamentally different from thermo-osmosis. Since the predicted flux closely agrees with the experiment, it is believed that the thermo-osmotic water transfer is negligibly small and the water transport mode within the PEM is dominated by a diffusion process, as proposed by Kim and Mench [9]. The transport mode in the PEM is further investigated through NR in the next section.

3.2 Through-Plane Water Distribution

The numerical model which calculates the water flux in the previous section is examined in more depth by inspecting the water content distribution in the through-plane direction. Figure 5(a) and (b) show the model predicted equivalent water thickness profiles for conditions listed in Table 1 (in solid lines) and their simulated NR water thicknesses after the blurring algorithm was applied (in dashed lines). The spatial resolution used in the NR simulation will be discussed below.

--

Figure 5

--

For the lower RH cases of 40 % and 64 %, no liquid saturation is predicted in the GDM and the slopes in the middle of the PEM are nearly flat or inclined towards the hot side, indicating a possible water flux in the direction of the hot side. In the case of 95 % RH on the hot side, there exists a point where the hot side gas reaches saturation inside the GDM and water condenses as the temperature drops in the direction of heat flux. For Case B, a saturation of 13 % is predicted at the PEM-GDM interface on the hot side. Given a sufficient humidity and a temperature drop, condensation occurs in the hot side GDM, raising the water content in the PEM towards the hot side and consequently an enhanced gradient is produced. A steeper slope is predicted for the larger temperature gradient of Case B, suggesting a higher water flux even though the relative humidity conditions are the same. The numerically predicted water distributions are then directly compared with those of the NR experiment.

A raw neutron radiograph of a dry reference is pictured in Figure 6(a) and an image histogram of a selected area derived from it is shown in the subset in Figure 7. The histogram captures a lateral distribution of the neutron intensity in the PEFC components, and from it, the locations and the interfaces of the PEM, the GDM, and the flow-field plates are evident. From the physical dimensions of the cell, the pixel pitch was found to be approximately 14.72 μm in the through-plane direction. Based on the procedure described in Section 2.2.1, the image derived spatial resolution for this particular experimental set is estimated to be about 68.8 μm by the error function fit to an interface of GDM-plate using the least-square method as shown in Figure 7. The sources of image degradation may come from observing an imperfect edge and misalignment of the sample to the neutron beam. This resolution is thus taken to be the worst case; therefore, 6 to 7 pixels in the vicinity of the center of the PEM are considered to represent the true water content of the PEM. Prior experiments revealed there was no evidence of change in neutron scattering cross-section by water within a PEM and beam-hardening effects for this detector were found negligible [10].

--

Figure 6

Figure 7

--

A processed (false colorized) image of the measured water thickness from Case B with 95 % RH shown in Figure 6(b) clearly shows the PEM containing the highest level of water and the GDM containing less liquid water. As a high gas flow is used, no observable liquid water in the channel is present in the image. Since one-dimensionality of the water transport (the horizontal direction in the image) can be assumed, the processed water thickness is vertically integrated along the uniform dimensions in the region indicated by the rectangular box in order to further reduce the random noise.

The resulting through-plane water distributions for Case A and B are plotted as dots in Figure 8(a) and (b), respectively. The intensity plots of the dry reference with corresponding temperature gradient are shown together to aid in locating the center of the PEM and the interfaces. The water distribution profiles, in terms of depth of measured water in millimeters, show the peaks occurring within the PEM. As the humidity in the hot side is raised, the water content in the PEM is seen to increase. A notable feature of the water distribution plots is the shift in the water content peak towards the hot side, especially for the high RH cases; an indication of the existence of a gradient in water content in the PEM. For the cases of 95 % RH, a visible rising slope of the water content towards the hot side in the PEM is detected. Additionally, with an increase in water content for the high humidity case seen in Case B, it may be indicative of an enhanced water flux with a larger temperature gradient.

--

Figure 8

--

The simulated water thickness distributions shown in Figure 5 are also superposed with the experimental data in Figure 8 as lines. A comparison of the profiles shows that the model is capable of quantitatively predicting the thickness of water to within the same order of magnitude and yield qualitatively similar characteristics as the experiment. The general trend of the profiles as well as the magnitude of the water content in the PEM is nearly in agreement with the experiment for 40 % and 64 % RHs, although the experimental results show nearly flat slopes. The model correctly predicts the increase in water content difference between inlet RH of 40 % and 64 % seen in the larger temperature gradient. The drop in water content level in the case of 40 % RH comes from a reduction in humidity of the cold side gas as a result of enhanced temperature gradient. For the 95 % RH cases, the model accordingly predicts the rising slopes of the water content gradient towards the hot side, however, at larger rates.

There are several discrepancies between the model predictions and the experiments. Most notably, the model overpredicts the water content both in the PEM and the GDM when the cell is highly humidified. The error in the model can be attributed to several factors, including the water uptake function and the water diffusivity used in the PEM as well as the properties of the GDM and the capillary relationship in porous media. Consider for example, a larger discrepancy in the predicted water content in the PEM than the experiment for the 95 % RH cases. It has been suggested that a compression force can reduce hydration of PEMs, especially at a higher humidification, and distribute water more uniformly [36]. Including the effect of the compression on the membrane water uptake may reduce such over-prediction. Additionally, the PEM is reported to swell up to 50 % of its dry thickness when wet [31] and may have effects in determining the thickness of water. This swelling is visible from the NR data in the PEM/GDM interfacial shift by 1 to 2 pixels. As the membrane expands into the GDM, the PFSA membrane density is reduced and subsequently the neutron attenuation due to the membrane.

Without taking into account of the change in the attenuation, it is possible to underestimate the thickness of water. Currently, a study is underway at the NIST to incorporate the neutron attenuation dependence in a free-swelling membrane [37].

In explaining the under-prediction of the water content values in the PEM for lower humidification conditions, it is conceivable that the effect of temperature is impacting significantly. It is well known that the membrane water uptake is sensitive to its temperature. Although there have been a few theoretical models of membrane hydration to temperature [38], except for the well-known water uptake data of Zawodwinski et al. at 30 °C [39], Zawodwinski et al. at 80 °C [40], and Hinatsu et al. at 80 °C [31] used in the present model, an experimental characterization of the water uptake isotherms at several temperatures is absent in the literature. The present model only uses the isotherm at 80 °C [31]. Additionally, the temperatures at the PEM-GDM interfaces affect vapor activity thus altering the membrane water uptake. Consideration of thermal and water transport interfacial resistances may further contribute to the thermal profile at the interfaces and subsequently to the water distribution.

An inspection of the water distribution within the cold side GDM and at the interface of GDM-plate shows very little liquid water for both cases, however, only minutely higher for higher humidity cases. While the numerical model predicts zero water present, the experimental data suggest evidence of condensation; thus possibly causing a weak PCI flow. Irreducible saturation may be occurring in the pockets of the hydrophilic carbon fiber, especially where compressed under the land.

In the GDM of the hot side, on the other hand, a more pronounced level of liquid water appears to be present at the GDM-plate interface and even in the channel. While some condensation of water is conceivable, we speculate that the detected water thickness is due to neutron attenuation by the GDM protruding into the channel. The higher humidity level at the PEM-GDM interface in the hot side swells the membrane; with especially the thick membrane used, an extra hygro-expansive force is asserted on the GDM. It is evident that the water detected at the interface is greater with increasing humidification as the membrane expands. The swelling of the PEM also shifts the PEM-GDM interfaces and contributes to a broadening of the profile peak, creating an additional artifact in the neutron radiograph. A larger volumetric expansion is unavoidable with the thick membrane used and is a trade-off in obtaining a reliable water depth within the PEM. Further, large neutron attenuation in a water-saturated PFSA membrane contributes to profile broadening, thus presently discerning the location of the interfaces of the PEM-GDM and the presence of saturation in the porous media near the interfaces is even more difficult and inconclusive.

The accuracy of the model depends on the accuracy of the material property characterization. Therefore, a rather simplistic representation of the material and transport property characterizations in our present model may be limiting and unable to extensively capture all the necessary details. These discrepancies between the model and the experiment raise renewed needs of improved material characterization and understanding, especially in wet conditions. Additionally, the model may lack certain transport processes that need to be incorporated. However, despite these shortfalls, the model is one of first of its kinds to successfully describe the through-plane water distribution and water transport qualitatively and quantitatively with the level of accuracy shown. These experimental results together with the numerical simulation strongly suggest that the water transport in the PEM under a temperature gradient is driven by a concentration gradient induced by the temperature difference.

4 Conclusions

An investigation of water transport across the PEM in a PEFC under a thermal gradient is performed through experiments of water balance measurement and high-resolution neutron radiography coupled with numerical modeling. From the water flux measurements, the water was found to be transported from the hot side to the cold side when the gases are sufficiently humidified. The water content distributions obtained from NR show the existence of a concentration gradient within the PEM, indicating the water transport in the direction from the hot side to the cold side when the inlet gases are sufficiently humidified; in agreement with the water flux measurements. The water content in the PEM was found to increase with increasing temperature gradient and possibly enhancing the water flux as well.

A one-dimensional, nonisothermal, two-phase numerical model based on the M^2 model was devised to complement the data obtained from the experiments. The model correctly predicted the water flux, except for highly humidified inlet gases. A comparison of the model to the NR experiment revealed the predicted water content is in reasonable qualitative agreement and at worst 50 % discrepant from the measured water content in the PEM. This discrepancy suggests a need of better material and transport characterizations for further improvement, especially under wet conditions. When improved material and transport properties are incorporated, the model is expected to further provide helpful insights into the transport phenomena.

While the high-resolution neutron radiography provided powerful and unique insights into the water distribution within the PEFC components in the through-plane direction *in situ*, several challenges remain to be addressed. Our analysis indicated the effect of channel/land in the flow-field cannot be ignored due to GDM protrusion caused by the membrane swelling. The effect possibly introduces an artifact in the inferred water thickness when the PEM is highly humidified. This issue may be partially alleviated by using narrower flow channels. The swelling of the membrane also shifts the PEM/GDM interface and makes the observation of water content in the PEM at those regions a challenge. A steep attenuation discontinuity at the interface of the PEM and the GDM poses another difficulty in accurately measuring the water in the GDM since blurring of the image is inevitable at the interface. A new MCP detector with 13 μm resolution has been implemented at the NIST and is expected to resolve some of the issues addressed above.

5 Acknowledgments

The authors acknowledge Mr. Eli Baltic of the NIST for technical assistance in carrying out the neutron radiography experiments and Nissan Motors, Ltd. for funding this research. This work was supported by the U.S. Department of Commerce, the NIST Ionizing Radiation Division, the Director's office of NIST, the NIST Center for Neutron Research, and the Department of Energy through interagency agreement no. DE-AI01-01EE50660.

6 References

1. S. K. Lee, K. Ito, T. Ohshima, S. Noda, and K. Sasaki, *Electrochem. Solid-State Lett.*, **12** (9) B126-B130 (2009).
2. M. Tasaka, T. Hirai, R. Kiyono, and Y. Aki, *J. Membr. Sci.,* **71** 151 (1992).
3. M. Tasaka and M. Nagasawa, *Biophysical Chemistry,* **8** 111 (1978).
4. J. P. G. Villaluenga, B. Seoane, V. M. Barragan, and C. Ruiz-Bauza, *J. Membr. Sci.*, **274** (1-2) 116 (2006).
5. R. Zaffou, H. R. Kunz, and J. M. Fenton, *ECS Trans.*, **3** (1) 909 (2006).
6. R. Zaffou, J. S. Yi, H. R. Kunz, and J. M. Fenton, *ECS Trans.*, **1** (6) 429 (2006).
7. R. Zaffou, J. S. Yi, H. R. Kunz, and J. M. Fenton, *Electrochem. Solid-State Lett.* **9** (9) A418 (2006).
8. S. Kim and M. M. Mench, *J. Membr. Sci.*, **328** (1-2) 113 (2009).
9. S. Kim and M. M. Mench, *J. Electrochem. Soc.*, **156** (3) B353 (2009).
10. D. S. Hussey, D. L. Jacobson, M. Arif, K. J. Coakley, and D. F. Vecchia, *J. Fuel Cell Sci. Technol.*, **7** 021024-1 (2010).
11. R. Satija, D. L. Jacobson, M. Arif and S. A. Werner, *J. Power Sources*, **129** (2) 238 (2004).
12. D. Kramer, J. Zhang, R. Shimoi, E. Lehmann, A. Wokaun, K. Shinohara, and G. G. Scherer, *Electrochim. Acta*, 50, 2603 (2005)
13. N. Pekula, K. Heller, P. A. Chuang, A. Turhan, M. M. Mench, J. S. Brenizer, and K. Ünlü, *Nucl. Instrum. Methods Phys. Res., Sect. A*, **542** (1-3) 134 (2005).
14. M. A. Hickner, N. P. Siegel, K. S. Chen, D. N. McBrayer, D. S. Hussey, D. L. Jacobson, and M. Arif, *J. Electrochem. Soc.*, **153** A902 (2006)

15. D. J. Ludlow, C. M. Calebrese, S. H. Yu, C. S. Dannehy, D. L. Jacobson, D. S. Hussey, and M. Arif, M. K. Jensen, and G.A. Eisman, *J. Power Sources* **162** 271–278 (2006).
16. M. A. Hickner, N.P. Siegel, K.S. Chen, D.S. Hussey, D.L. Jacobson, and M. Arif, *J. Electrochem. Soc.*, **155** (3) B294 (2008).
17. J. Park, X. Li, D. Tran, T. Abdel-Baset, D. S. Hussey, D. L. Jacobson and M. Arif, *Int. J. Hydrogen Energy*, **33** (13) 3373 (2008).
18. D. Spernjak, S. G. Advani, and A. K. Prasad, *J. Electrochem. Soc.*, **156** (1) B109 (2009).
19. R. J. Bellows, M. Y. Lin, M. Arif, A. K. Thompson, and D. Jacobson, *J. Electrochem. Soc.*, **146** (3) 1099 (1999)
20. D. S. Hussey, D. L. Jacobson, M. Arif, J. P. Owejan, J. J. Gagliardo, and T. A. Trabold, *J. Power Sources*, **172** 225–228 (2007)
21. M. A. Hickner, N. P. Siegel, K. S. Chen, D. S. Hussey, D. L. Jacobson, and M. Arif, *J. Electrochem. Soc.*, **155** (4) B427 (2008).
22. A. Z. Weber and M. A. Hickner, *Electrochim. Acta*, **53** (26) 7668 (2008).
23. J. S. Spendelow, R. Mukundan, J. R. Davey, T. Rockward, D. S. Hussey, D. L. Jacobson, M. Arif, and R. L. Borup, *ECS Trans.*, **16** (2) 1345-1355 (2008)
24. A. Turhan, S. Kim, M. Hatzell, and M. M. Mench, *Electrochim. Acta*, **55** 2734–2745 (2010)
25. C. Y. Wang and P. Cheng, *Int. J. Heat Mass Transfer*, **39** (17) 3607-3618 (1996).
26. C. Y. Wang and P. Cheng, in *Adv. Heat Transfer*,J. P. Hartnett, T. F. Irvine, Jr., Y. I. Cho, G.A. Greene, Editors, **30**, p. 93, Academic Press, San Diego (1997).

27. U. Pasaogullari and C. Y. Wang, *Electrochim. Acta*, **49** (25) 4359 (2004).
28. U. Pasaogullari and C. Y. Wang, *J. Electrochem. Soc.*, **152** (2) A380 (2005).
29. U. Pasaogullari, C. Y. Wang, and K. S. Chen, *J. Electrochem. Soc.*, **152** (8) A1574 (2005).
30. H. Ju, G. Luo, and C. Y. Wang, *J. Electrochem. Soc.*, **154** (2) B218-B228 (2007).
31. J. T. Hinatsu, M. Mizuhata, and H. Takenaka, *J. Electrochem. Soc.*, **141** (6) 1493-1498 (1994).
32. S. Motupally, A. J. Becker, and J. W. Weidner, *J. Electrochem. Soc.*, **147** (9) 3171-3177 (2000).
33. M. Khandelwal and M. M. Mench, *J. Power Sources*, **161** (2) 1106 (2006).
34. Toray manufacturer specifications, http://www.torayca.com
35. G. Dougherty and Z. Kawaf, *Radiography*, **7** 255–262 (2001).
36. I. Nazarov and K. Promislow, *J. Electrochem. Soc.*, **154** (7) B623-B630 (2007).
37. D. Spernjak, P. Mukherjee, R. Mukundan, J. Davey, D. Hussey, D. Jacobson, and R. Borup, *218th ECS Meeting*, Abstract #717 (2010).
38. A. Z. Weber and J. Newman, *J. Electrochem. Soc.*, **150** (7) A1008-A1015 (2003).
39. T. A. Zawodzinski, M. Neeman, L. O. Sillerud, and S. Gottesfeld, *J. Phys. Chem.*, 95 (**15**) 6040-6044 (1991).
40. T. A. Zawodzinski and C. Derouin, *J. Electrochem. Soc.*, **140** (4) 1041-1047 (1993)

Table 1. Neutron radiography PEFC experimental conditions.

Case	A		B	
Plate	Cold	Hot	Cold	Hot
Temperature	62 °C	70 °C	50 °C	70 °C
Relative Humidity	95 % (DP = 61 °C)	40 % (DP = 50 °C) 64 % (DP = 60 °C) 95 % (DP = 69 °C)	95 % (DP = 49 °C)	40 % (DP = 50 °C) 64 % (DP = 60 °C) 95 % (DP = 69 °C)
Pressure	Ambient		Ambient	

Table 2. Specifications of neutron radiography imaging.	
Aperture (x : height, y : width)	x : 1 mm, y : 10 mm
Active area-Detector distance	21 mm (including MCP thickness)
Detector-Aperture Distance	6 m
Detector Pixel Pitch	14.72 μm
Detector Resolution (intrinsic)	25 μm
Data acquisition time	60 s / image
Water attenuation coefficient	0.338 mm^{-1}

Table 3. Numerical Model Governing Equations.

In the diffusion media region:		
Mass	$\frac{d}{dx}\left(\rho u\right)=0$	(8)
Species	$\frac{d}{dx}\left(\gamma_c^i u C^i\right)=\frac{d}{dx}\left(D_g^{i,eff}\frac{dC_g^i}{dx}\right)-\frac{d}{dx}\left[\left(\frac{\omega_l^i}{M^i}-\frac{C_g^i}{\rho_g}\right)\mathbf{j_l}\right]+\frac{d}{dx}\left[D_i^{\mathrm{H_2O,eff}}\frac{dC_{\mathrm{sat}}^{\mathrm{H_2O}}}{dT}\frac{dT}{dx}\right]$	(9)
Energy	$\frac{d}{dx}\left(\gamma_h \rho c_p u T\right)=\frac{d}{dx}\left(k^{eff}\frac{dT}{dx}\right)-\frac{d}{dx}\left(h_{fg} j_l\right)$	(10)
In the membrane region:		
Water	$0=\frac{d}{dx}\left(D_\lambda \frac{\rho_{dry}}{EW}\frac{d\lambda}{dx}\right)$	(11)
Energy	$0=\frac{d}{dx}\left(k^{eff}\frac{dT}{dx}\right)$	(12)

Table 4. Transport and Material Properties.

Description	Value	Reference
Transport Properties		
Surface tension, σ	0.0625 N m^{-1}	[27]
Gas kinematic viscosity, υ_g	1.76×10^{-5} m^2 s^{-1}	
Liquid kinematic viscosity, υ_l	3.52×10^{-7} m^2 s^{-1}	
Material Properties		
Nafion dry density	1980 kg m^{-3}	
Nafion equivalent weight	1.1 kg mol^{-1}	
Nafion thermal conductivity	0.25 W m^{-1} K^{-1}	[33]
Porosity (uncompressed)	0.78	[34]
GDM absolute permeability, K	8.69×10^{-12} m^2	
GDM contact angle, θ_c	80°	
GDM thermal conductivity	1.0 W m^{-1} K^{-1}	

Figure Captions

Figure 1: A schematic diagram of experimental setup of water transport measurement.

Figure 2: Cell hardware for neutron radiography experiments.

Figure 3: Through-plane temperature measurement and numerical prediction. Temperatures at the hot and cold side separator plates and the interface of PEM and cold-side GDM are shown in data points. Numerically calculated temperature profiles are shown in solid lines.

Figure 4: Measurement of water flux experiment across Nafion NE1110 under a temperature gradient shown as data points and numerical simulation shown in line. T_C = 35.5 °C and T_H = 74.2 °C. T_C = 100 % and RH_H = varied.

Figure 5: Numerically predicted water thicknesses (solid curves) and corresponding neutron radiography blurring simulation (dashed curves) of conditions listed in Table 1.

Figure 6: (a) A raw neutron radiograph of a dry reference, and (b) a false colorized image of water thickness of Case B at RH 95 %. The GDM is 6 mm wide in the neutron beam direction.

Figure 7: Neutron intensity of a dry state reference image and the error function (ERF) model fit.

Figure 8: Through-plane water thickness profiles of neutron radiography experimental measurements (points) and corresponding numerical model simulations (lines) for conditions given in Table 1.

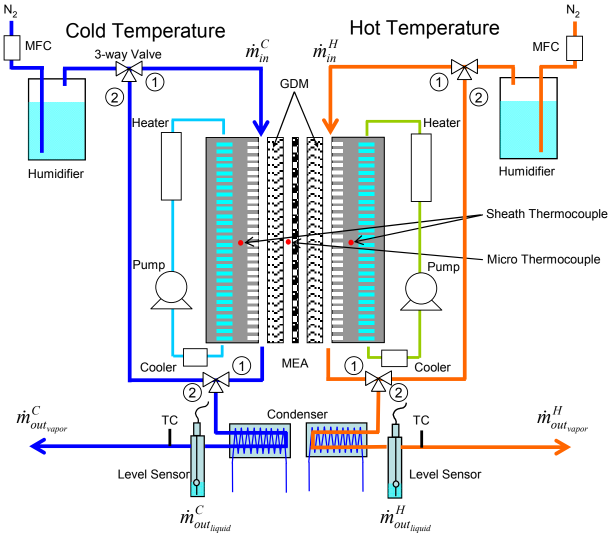

N_2
MFC
Cold Temperature
3-way Valve
②
①
$\dot{m}_{in}^{C}$
GDM
$\dot{m}_{in}^{H}$
Hot Temperature
N_2
MFC
①
②
Humidifier
Heater
Heater
Humidifier
Sheath Thermocouple
Micro Thermocouple
Pump
Pump
Cooler
①
MEA
①
Cooler
②
②
$\dot{m}_{out_{vapor}}^{C}$
TC
Condenser
TC
$\dot{m}_{out_{vapor}}^{H}$
Level Sensor
Level Sensor
$\dot{m}_{out_{liquid}}^{C}$
$\dot{m}_{out_{liquid}}^{H}$

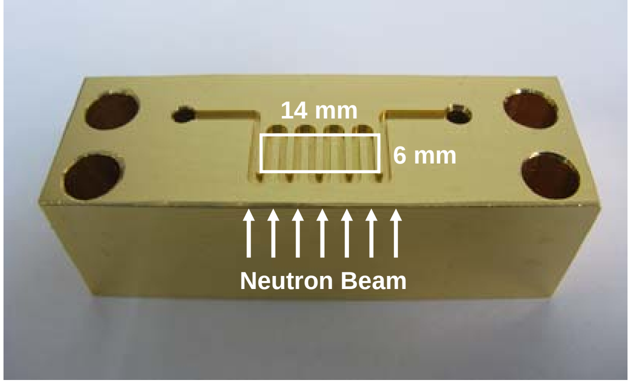
14 mm
6 mm
Neutron Beam

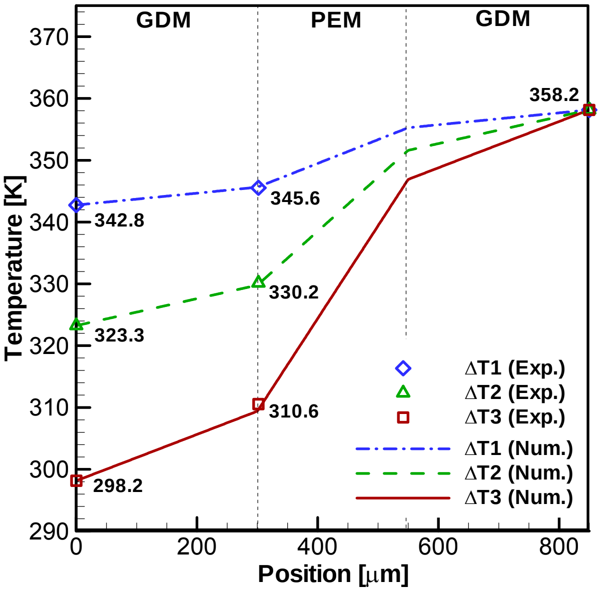
GDM
PEM
GDM
370
360
350
340
330
320
310
300
290
Temperature [K]
0
200
400
600
800
Position [μm]
358.2
342.8
345.6
323.3
330.2
310.6
298.2
ΔT1 (Exp.)
ΔT2 (Exp.)
ΔT3 (Exp.)
ΔT1 (Num.)
ΔT2 (Num.)
ΔT3 (Num.)

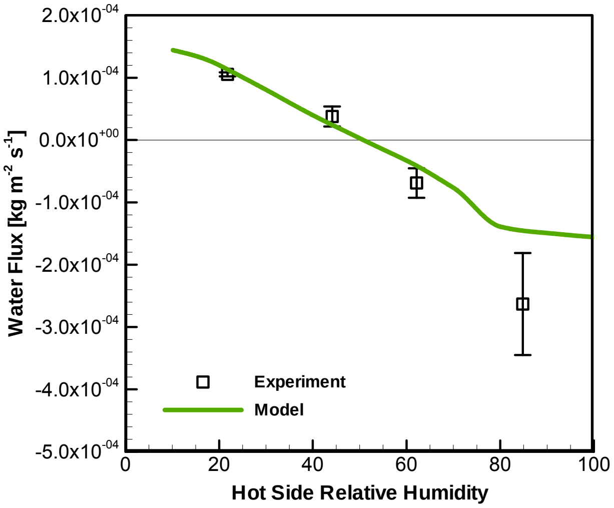
2.0x10^-04
1.0x10^-04
0.0x10^+00
-1.0x10^-04
-2.0x10^-04
-3.0x10^-04
-4.0x10^-04
-5.0x10^-04
Water Flux [kg m^-2 s^-1]
0
20
40
60
80
100
Hot Side Relative Humidity
Experiment
Model

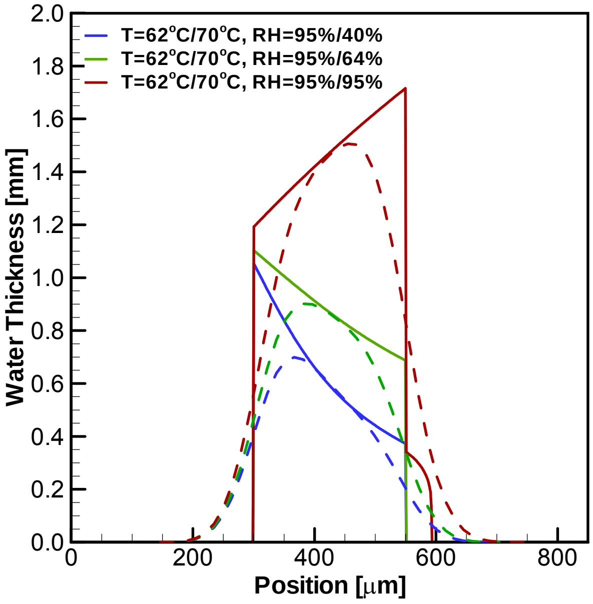

(a) Case A

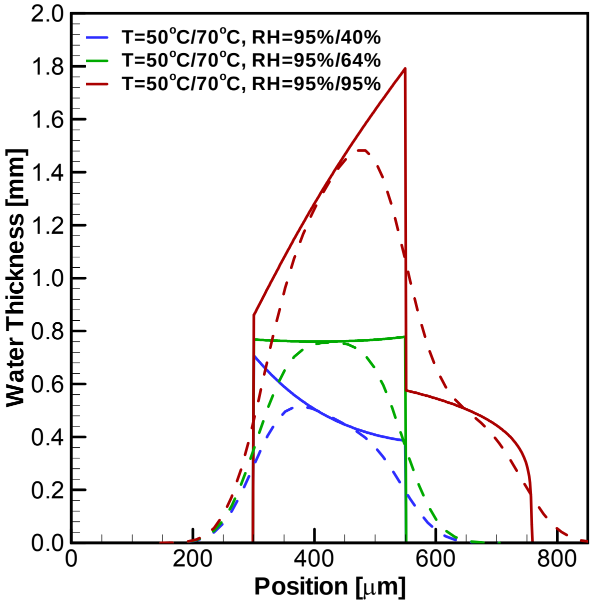

(b) Case B

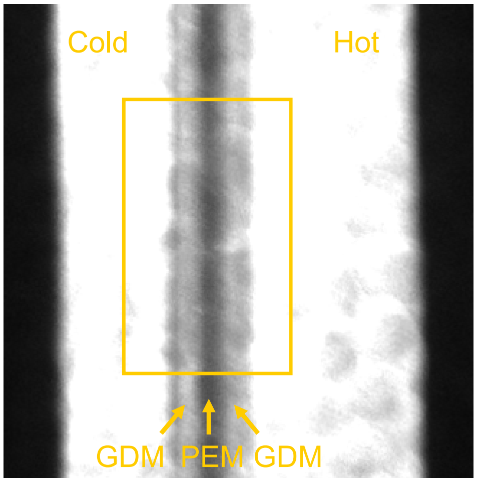
Cold
Hot
GDM
PEM
GDM

(a)

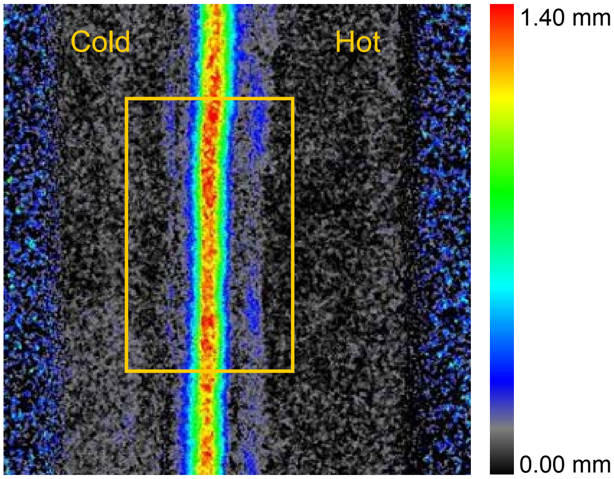

(b)

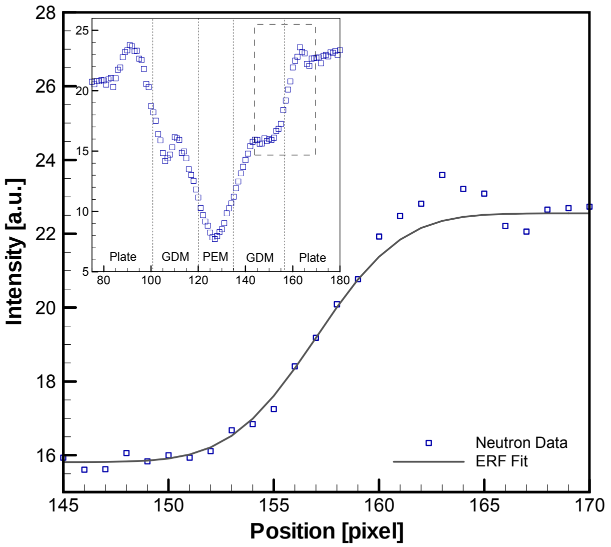
28
26
24
22
20
18
16
Intensity [a.u.]
145
150
155
160
165
170
Position [pixel]
Neutron Data
ERF Fit
25
20
15
10
5
80
100
120
140
160
180
Plate
GDM
PEM
GDM
Plate

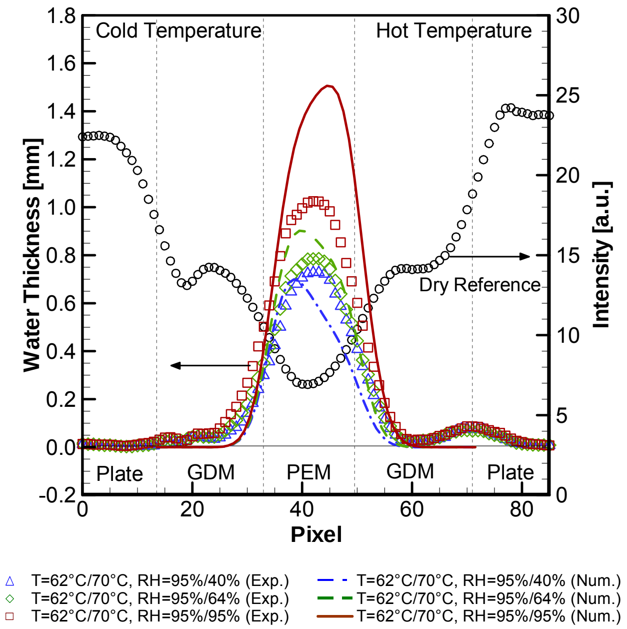

(a) Case A

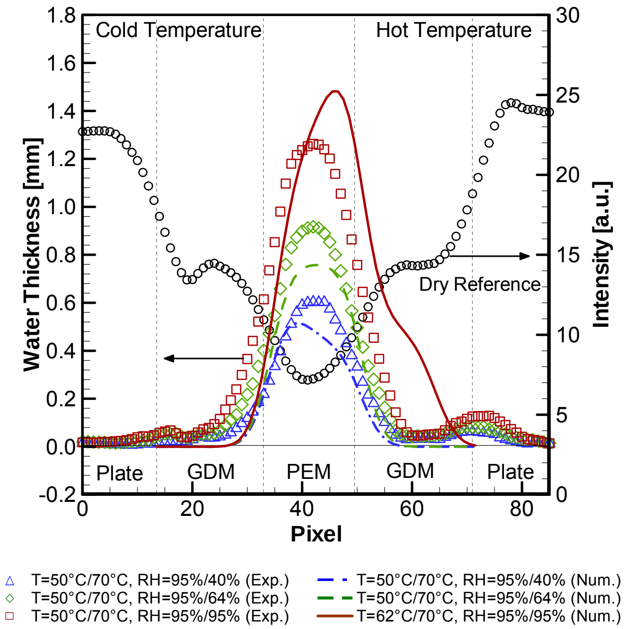

(b) Case B